

The Effects of Numerical Dissipation on Hurricane Rapid Intensification with Observational Heating

M. B. Hasan¹, S. R. Guimond², M. L. Yu¹, S. Reddy³, and F. X. Giraldo³

¹Department of Mechanical Engineering, University of Maryland, Baltimore County, Baltimore, MD, USA

²Joint Center for Earth Systems Technology and Department of Physics, University of Maryland,
Baltimore County, Baltimore, MD, USA

³Department of Applied Mathematics, Naval Postgraduate School, Monterey, CA, USA

Key Points:

- The WRF dynamic core dissipates $\sim 20\%$ more kinetic energy than NUMA for a dry vortex forced by four-dimensional latent heating observations.
- Values of the eddy diffusivity in WRF need to be reduced by $\sim 50\%$ from those in NUMA in order to produce a similar intensity time series.
- Budgets and sensitivity tests indicate that the low-order approximation of the pressure gradient is the source of the dissipation in WRF.

Corresponding author: M. B. Hasan, mbadhrh1@umbc.edu

Corresponding author: S. R. Guimond, sguimond@umbc.edu

Abstract

The computational fluid dynamics of hurricane rapid intensification (RI) is examined through idealized simulations using two codes: a community-based, finite-difference/split-explicit model (WRF) and a spectral-element/semi-implicit model (NUMA). The focus of the analysis is on the effects of implicit numerical dissipation (IND) in the energetics of the vortex response to heating, which embodies the fundamental dynamics in the hurricane RI process. The heating considered here is derived from observations: four-dimensional, fully nonlinear, latent heating/cooling rates calculated from airborne Doppler radar measurements collected in a hurricane undergoing RI. The results continue to show significant IND in WRF relative to NUMA with a reduction in various intensity metrics: (1) time-integrated, mean kinetic energy values in WRF are $\sim 20\%$ lower than NUMA and (2) peak, localized wind speeds in WRF are $\sim 12\text{m/s}$ lower than NUMA. Values of the eddy diffusivity in WRF need to be reduced by $\sim 50\%$ from those in NUMA to produce a similar intensity time series.

Kinetic energy budgets demonstrate that the pressure contribution is the main factor in the model differences with WRF producing smaller energy input to the vortex by $\sim 23\%$, on average. The low-order spatial discretization of the pressure gradient in WRF is implicated in the IND. In addition, the eddy transport term is found to have a largely positive impact on the vortex intensification with a mean contribution of $\sim 20\%$. Overall, these results have important implications for the research and operational forecasting communities that use WRF and WRF-like numerical models.

Plain Language Summary

The intensity of a hurricane is primarily a balance between energy production and dissipation from various physical processes. Numerical models calculate this energy balance by solving complicated equations that attempt to capture these physical processes. Previous research has shown that the methods used to solve these equations can introduce additional dissipation into the system that affects the prediction of the storm intensity. In this paper, we examine this “numerical dissipation” idea more closely by conducting carefully designed comparisons between the community numerical model (WRF) and an advanced, research model (NUMA). Using observational estimates of heating in clouds, which feed the production of energy, we find that the WRF model produces significantly more numerical dissipation relative to NUMA that results in a reduced intensity of the storm. Our analysis indicates that the reason for the anomalous numerical dissipation in WRF is due to how the pressure gradient is computed. These results can have potentially important consequences for operational forecasts, especially the rapid intensification process. For example, the under-prediction or low bias of rapid intensification forecasts may be partly due to excessive numerical dissipation.

1 Introduction

The record-breaking 2020 Atlantic hurricane season and recent storms that leveled the Florida panhandle in 2018 (Hurricane Michael) and submerged parts of Texas in 2017 (Hurricane Harvey) illustrate the devastating impacts of these systems, even in the modern era. Unfortunately, as the climate system continues to warm, recent research suggests that intense hurricanes will likely become more common, produce more flooding rainfall, and last longer even after landfall (Knutson et al., 2015, 2019; Li & Chakraborty, 2020). As a result, hurricanes will likely place increasing stress on many sectors of society for various countries across the globe.

Accurate forecasting of hurricane track, intensity, storm surge, and rainfall from dynamical models can mitigate losses by facilitating disaster preparations and evacua-

63 tions that can save lives and billions of dollars in damages. However, the operational pre-
64 diction of hurricane intensity, especially rapid intensification (RI), has been mainly stag-
65 nant (Marks & Shay, 1998; Rappaport et al., 2009), with large forecast errors still present
66 today (DeMaria et al., 2014). As described in DeMaria et al. (2014), none of the deter-
67 ministic models had RI forecasting capability from 1991 to around 2015. There has been
68 some ability to forecast RI with both dynamical and statistical models since 2015, how-
69 ever, a significant under-prediction or low bias in RI cases is still present today (DeMaria
70 et al., 2021).

71 The increase of kinetic energy in hurricane intensification, as well as RI, is driven
72 by the vortex response to heating in convective clouds (e.g., Shapiro & Willoughby, 1982),
73 where the source of moist enthalpy flux comes from the thermodynamic disequilibrium
74 between the ocean and atmosphere, (e.g., Emanuel, 1986). Dissipation of energy occurs
75 most prominently in the boundary layer through surface friction and a hierarchy of tur-
76 bulent eddies of various scales. However, new research has shown that the hurricane bound-
77 ary layer is not purely dissipative and contains coherent turbulent structures that can
78 “backscatter” energy to larger scales (Sroka & Guimond, 2021). In numerical models,
79 dissipation of energy can also occur implicitly through the algorithms used to solve the
80 fluid-flow equations (“implicit numerical dissipation”) or explicitly through the addition
81 of filters. Implicit numerical dissipation can occur from the use of low-order discretiza-
82 tions of the governing equations in both space and time. For example, the use of second-
83 order or upwind-biased spatial discretizations of the advective terms can result in sub-
84 stantial numerical dissipation error when compared to high-order (e.g., fifth) or centered
85 schemes (Hoffman & Frankel, 2001; Skamarock & Klemp, 2008)).

86 In general, minimal numerical dissipation is desired in highly nonlinear computa-
87 tional fluid dynamics problems, such as hurricanes, because errors incurred from exces-
88 sive dissipation can quickly propagate through the system. Kravchenko and Moin (1997)
89 examined numerical errors in spectral and finite difference codes as well as the effects
90 of sub-grid scale models in turbulent channel flow. They demonstrated that the high wavenum-
91 ber portion of the energy spectrum is severely damped by truncation errors in low-order
92 (e.g., second) finite-difference schemes, and the contribution of the sub-grid scale model
93 is small in this context. By increasing the order of the finite-difference approximations,
94 the results of their large eddy simulations and the performance of the sub-grid scale model
95 were enhanced. Larsson et al. (2007) found that maintaining low numerical dissipation
96 was important for simulating shock/turbulence interactions, especially for coarse reso-
97 lution simulations where the fields are under-resolved and a sub-grid model is required
98 (this is also the case in mesoscale atmospheric modeling). In these under-resolved sim-
99 ulations, the numerical dissipation was large enough to dampen or erase the smaller-scale
100 motions on the grid and from the sub-grid model.

101 Continuous Galerkin (CG) and discontinuous Galerkin (DG) numerical methods
102 have several unique properties which distinguish them from low-order (i.e., the order of
103 accuracy equal to or smaller than two) methods and other high-order methods, such as
104 finite volume/difference schemes. These include: 1) possessing low dissipation and dis-
105 persion errors for turbulent flows with highly disparate spatial and time scales; 2) achiev-
106 ing arbitrary high-order discretization for all spatial derivatives; and 3) highly scalable,
107 and efficient on massively parallel supercomputers, such as those accelerated by Graph-
108 ics Processing Units (GPUs) (Abdi et al., 2017, 2019). These superior numerical prop-
109 erties make high-order CG and DG methods attractive for hurricane research. The ad-
110 vantages of high-order numerical methods over their low-order counterparts for low Reynolds
111 number flow problems has been demonstrated through a workshop series, The Interna-
112 tional Workshop on High-Order CFD Methods (Wang et al., 2013). However, when sim-
113 ulating under-resolved problems that require a sub-grid turbulence model and problems
114 with discontinuities, high-order numerical schemes can have issues with excessive grid
115 scale noise, aliasing and stability (Honein & Moin, 2004; Gassner & Beck, 2013; Moura

116 et al., 2017). These issues can lead to errors in the simulated flow or a failure of the sim-
 117 ulation. To address these potential problems, de-aliasing techniques (Blaisdell et al., 1996;
 118 Gassner, 2013; Karamanos & Karniadakis, 2000; Fischer & Mullen, 2001; Gassner & Beck,
 119 2013), localized artificial viscosity (Persson & Peraire, 2006; Yu et al., 2015) and limiters
 120 (Cockburn & Shu, 1998; Qiu & Shu, 2005; Zhang & Shu, 2010) can be used to stabilize
 121 flow simulations. In this study, we rely on a combined approach that applies artificial
 122 viscosity based on output from a turbulent kinetic energy (TKE) sub-grid model for tur-
 123 bulent diffusion; see details in Section 2.3.

124 Takemi and Rotunno (2003) studied the effects of sub-grid mixing and numerical
 125 filtering in squall line simulations using the Weather Research and Forecasting (WRF)
 126 model, which is a finite difference based code that can provide high order discretization
 127 for the advective (or flux divergence) terms only (Skamarock & Klemp, 2008). The au-
 128 thors found that using a fifth-order, upwind-biased advection scheme along with a stan-
 129 dard TKE sub-grid model resulted in many noisy, grid-scale convective cells. Rather than
 130 applying an explicit numerical filter, which could damage the physical modes, the au-
 131 thors tuned the TKE sub-grid model coefficient to produce reasonable convective struc-
 132 tures and energy scaling with wavelength. They also tested the inclusion of an explicit
 133 numerical filter and found that it had a much larger effect on the solutions than the sub-
 134 grid TKE model, which highlights the importance of analyzing numerical dissipation.
 135 It is clear that in order to ensure both high accuracy and stability of a simulated flow,
 136 a careful balance between signal and noise must be achieved.

137 In a theoretical hurricane study, Guimond et al. (2016) showed that the vortex re-
 138 sponse to simple, impulsive, asymmetric thermal anomalies can produce significant dif-
 139 ferences in system intensity across models due to the amount of implicit numerical dis-
 140 sipation. The community atmospheric model (WRF) was shown to have anomalously
 141 large implicit numerical dissipation when compared to research atmospheric codes [the
 142 High-Gradient (HIGRAD) model and the Non-hydrostatic Unified Model of the Atmo-
 143 sphere (NUMA)], which resulted in a muted intensity response from asymmetric ther-
 144 mal anomalies. The HIGRAD and NUMA models produced a more energetic response
 145 due to much less numerical dissipation. Spectral kinetic energy budgets showed that the
 146 pressure gradient term was the dominant source of the anomalous dissipation in WRF
 147 with the flux of inertia-gravity wave energy describing most of the variance in the pres-
 148 sure term. Acoustic and inertia-gravity waves are considered fast modes in the equation
 149 set, which are split off from the slow modes in WRF. This understanding lead to the rec-
 150 ommendation that the time integration scheme was the main culprit for the numerical
 151 dissipation in WRF. Evidence for this hypothesis was shown through sensitivity tests
 152 with different time integration schemes in NUMA, which showed significant differences
 153 in the amount of energy and role of the pressure term.

154 In this work, we study the response of a tropical storm-like vortex to time-dependent,
 155 3-D observational heating calculated from airborne Doppler radar measurements in the
 156 RI of Hurricane Guillermo (1997). The remainder of the paper is organized as follows.
 157 In Section 2, a detailed description of the numerical models and simulation setup is pre-
 158 sented. Therein, we introduce the WRF and NUMA models, vortex initialization and
 159 heating strategies, and eddy viscosity and diffusivity setup. Comparison of the wind field
 160 features, e.g., maximum and azimuthal mean wind speed as well as kinetic energy, from
 161 WRF and NUMA is discussed in Section 3. In this section, we also present kinetic en-
 162 ergy budget analyses to explain the wind field disparity between WRF and NUMA. Im-
 163 portant implications of this work in the hurricane research and operational fields are given
 164 in Section 4. Future work is also discussed in this section.

2 Description and setup of numerical models

A comprehensive introduction of the governing equations and numerical methods used in the WRF-ARW (hereafter WRF) and NUMA models have been given in Guimond et al. (2016). For completeness, we briefly review them below.

2.1 The WRF Model

The WRF model solves the compressible, non-hydrostatic Euler equations in a conservative form with a η mass vertical coordinate (Laprise, 1992; Skamarock & Klemp, 2008). For comparisons with NUMA, all variables are interpolated to regular height levels in post-processing. Note that the differences between the η levels and height are very small for these idealized simulations. The simplified model equations for a dry atmosphere can be expressed as follows, using a Laplacian operator for explicit diffusion and η as the vertical coordinate:

$$\frac{\partial mu}{\partial t} + \nabla \cdot (m\mathbf{u}u) = -\frac{m}{\rho} \frac{\partial \hat{p}}{\partial x} + fmv + \nabla \cdot (m\mu\nabla u) \quad (1)$$

$$\frac{\partial mv}{\partial t} + \nabla \cdot (m\mathbf{u}v) = -\frac{m}{\rho} \frac{\partial \hat{p}}{\partial y} - f\mu u + \nabla \cdot (m\mu\nabla v) \quad (2)$$

$$\frac{\partial mw}{\partial t} + \nabla \cdot (m\mathbf{u}w) = g \left(\frac{\partial \hat{p}}{\partial \eta} - \hat{m} \right) + \nabla \cdot (m\mu\nabla w) \quad (3)$$

$$\frac{\partial m\theta}{\partial t} + \nabla \cdot (m\mathbf{u}\theta) = S + \nabla \cdot (m\kappa\nabla \hat{\theta}) \quad (4)$$

$$\frac{\partial m}{\partial t} + \nabla \cdot (m\mathbf{u}) = 0. \quad (5)$$

Here u, v and w are the velocities in three dimensions, $m = m(x, y)$ is the mass per unit area within a column, θ is the potential temperature, ρ is the dry air density, \hat{p} is the perturbation pressure, f is the Coriolis parameter, g is gravity, μ is the eddy viscosity, κ is the thermal diffusivity, S is the heating rate source term, and ∇ is the three-dimensional gradient operator. Variables with a hat denote perturbations from the hydrostatically balanced reference state.

A combined finite-difference/finite-volume spatial discretization of the governing equations is employed in WRF. In the horizontal and vertical directions, a spatially staggered Arakawa C grid is utilized where velocities are defined on the cell faces and scalars at the cell centers. For the nonlinear advective terms, a fifth-order, upwind-biased discretization in the horizontal and a third-order scheme in the vertical are typically used. We have utilized these settings here, but also tested the impacts of the less diffusive, even-ordered schemes (sixth-order and fourth-order in the horizontal and vertical dimensions, respectively). The differences between the even-ordered and odd-ordered schemes were small (maximum values of +/- 0.5 m/s in the eyewall) and therefore, we utilize the odd-ordered formulations in all presented results. The WRF model relies on a split-explicit time integration process, where acoustic and gravity wave modes are calculated using a small time step and advection is computed on a larger time step (Klemp & Wilhelmson, 1978; Wicker & Skamarock, 2002; Skamarock & Klemp, 2008). Horizontal modes are solved explicitly within the small time stage, while vertical modes are implicitly solved. The implicit solve is done with backward Euler. A third-order Runge-Kutta scheme is used to perform the overall time integration, including both the small- and large-time step equations. The small time step results are applied as a correction to the large time step calculations during the Runge-Kutta time integration. More details on WRF can be found in (Skamarock & Klemp, 2008). Finally, we seek to produce minimally dissipative WRF solutions and therefore, we have turned *off* all filtering/damping options:

208 explicit sixth-order numerical filtering, vertical velocity damping, divergence damping
 209 and external mode damping. Artificial viscosity is applied at the model top and through
 210 the Laplacian operators in the above equations are discussed further in Section 2.3.

211 2.2 The NUMA Model

212 The NUMA model is capable of using various forms of the Euler equations [e.g.,
 213 Giraldo and Restelli (2008), Giraldo et al. (2010)]. However, for this study, we use the
 214 non-conservative form using potential temperature as the thermodynamic variable [Kelly
 215 and Giraldo (2012), Giraldo et al. (2013)] to be consistent with Guimond et al. (2016).
 216 The choice of conservative or non-conservative equation set is not expected to make a
 217 significant difference because the error resulting from the non-conservative set is much
 218 lower than the temporal error (Giraldo & Restelli, 2008). Instead of the η mass verti-
 219 cal coordinate, physical height z is used in NUMA. The governing equations are expressed
 220 as:

$$221 \quad \frac{\partial u}{\partial t} + \mathbf{u} \cdot \nabla u = -\frac{1}{\rho} \frac{\partial \hat{p}}{\partial x} + fv + \nabla \cdot (\mu \nabla u) \quad (6)$$

$$222 \quad \frac{\partial v}{\partial t} + \mathbf{u} \cdot \nabla v = -\frac{1}{\rho} \frac{\partial \hat{p}}{\partial y} - fu + \nabla \cdot (\mu \nabla v) \quad (7)$$

$$223 \quad \frac{\partial w}{\partial t} + \mathbf{u} \cdot \nabla w = -\frac{1}{\rho} \frac{\partial \hat{p}}{\partial z} - \frac{\hat{\rho}}{\rho} g + \nabla \cdot (\mu \nabla w) \quad (8)$$

$$224 \quad \frac{\partial \theta}{\partial t} + \mathbf{u} \cdot \nabla \theta = S + \nabla \cdot (\kappa \nabla \hat{\theta}) \quad (9)$$

$$225 \quad \frac{\partial \rho}{\partial t} + \nabla \cdot (\rho \mathbf{u}) = 0 \quad (10)$$

226 The spatial discretization of Eqs. (6)-(10) is carried out using the CG spectral el-
 227 ement method (CG-SEM) (Giraldo & Restelli, 2008; Giraldo et al., 2013; Giraldo, 2020).
 228 Specifically, the physical domain is decomposed into a set of non-overlapping hexahe-
 229 dral elements and inside each element, the state variables are represented by polynomial
 230 expansion using Lagrange basis functions of a chosen order. The continuous spatial deriva-
 231 tives are constructed in discrete form by analytically taking derivatives of the polyno-
 232 mials that approximate the solutions. The state variables in each element are collocated
 233 with each other and placed at unequally spaced Legendre-Gauss-Lobatto points. In this
 234 study, we utilize fifth-order polynomial basis functions in all three spatial dimensions,
 235 which also provides fifth-order accuracy for all spatial derivatives and is identical to that
 236 presented in Guimond et al. (2016). Note that the stencil for all polynomial orders in
 237 NUMA is symmetric about the element centroid, so upwind-biased diffusion for fifth-order
 238 polynomials is not present. For time integration, the three-dimensional semi-implicit method-
 239 ology (Giraldo et al., 2013) is used along with a second-order leapfrog scheme (LF2). A
 240 first-order Robert-Asselin time filter is applied to stabilize the LF2 scheme. The above
 241 description of NUMA comprises our control simulations. Several other time integration
 242 formulations are available in NUMA and we will note where sensitivity tests have been
 243 conducted. Interested readers are referred to Giraldo and Restelli (2008); Giraldo et al.
 244 (2013) for more details of the NUMA model.

245 2.3 Details of Simulation Setup

246 Careful analysis has been undertaken to setup WRF and NUMA nearly exactly the
 247 same to isolate any differences in the model solutions to the numerical schemes that com-
 248 prise the dynamic core. The computational domain is a box extending 800 *km* in the
 249 horizontal directions and 20 *km* in the vertical direction. In WRF, 2 *km* grid spacing

250 in the horizontal is chosen to match that of the radar observations used as forcing and
 251 to be consistent with Guimond et al. (2016). The first model level is found at 167 *m* with
 252 constant vertical spacing of 333 *m* up to the model top (60 levels). To match the hor-
 253 izontal and vertical grid spacing in WRF, we have used 80 elements in each horizontal
 254 direction and 12 elements in the vertical direction along with fifth-order polynomials in
 255 all dimensions for the NUMA grid, as described in Section 2.2. These settings yield an
 256 element-averaged grid spacing in NUMA of ~ 2 *km* in the horizontal and ~ 333 *m*
 257 in the vertical. A time step of 2 seconds is used in each model.

258 Periodic boundary conditions are used in both horizontal directions in each model.
 259 A gravity wave absorbing zone (sine-squared function) is imposed at the top of the com-
 260 putational domain with the WRF zone occupying the top 4 *km* along with a small co-
 261 efficient (0.00833) and the NUMA zone representing the top 1 *km* with a large coeffi-
 262 cient (1.0). The differences in the absorbing zones are due to stability issues and sen-
 263 sitivity tests show the results are not sensitive to these choices. The free-slip boundary
 264 condition is applied at the bottom of the computational domain in each model, which
 265 disables fluxes of quantities (such as heat) from the surface and prevents a frictional bound-
 266 ary layer from developing. These idealizations enable the focus to be on the vortex dy-
 267 namic response to the imposed heating. The simulations are run without moisture, but
 268 instead, four-dimensional latent heating/cooling rates derived from airborne Doppler radar
 269 observations are used to force the model as described below.

270 In post-processing, both WRF and NUMA fields are interpolated to a uniform, col-
 271 located grid at the horizontal/vertical grid spacings listed above. Linear interpolation
 272 is used to post-process the WRF results. To post-process NUMA results, a high-order
 273 interpolation based on Lagrange polynomials is applied, which is facilitated by the spec-
 274 tral element method (since by construction the solution exists everywhere in the element).
 275 To ease interpolation, any hexahedral element in the physical space (x, y, z) can be trans-
 276 formed into a standardized space $(\alpha, \beta, \gamma) \in [-1, 1] \times [-1, 1] \times [-1, 1]$. Thus, for any
 277 N th-order standard hexahedral element, there are $N+1$ Legendre-Gauss-Lobatto points,
 278 namely, $(\alpha_i, \beta_i, \gamma_i)$, $i = 1, \dots, N+1$, in each direction α , β and γ . The Lagrange poly-
 279 nomial basis $L_{IJK}(\alpha, \beta, \gamma)$, $I, J, K = 1, \dots, N+1$, can be constructed using the ten-
 280 sor product as

$$281 \quad L_{IJK}(\alpha, \beta, \gamma) = \left(\prod_{i=1, i \neq I}^{N+1} \frac{\alpha - \alpha_i}{\alpha_I - \alpha_i} \right) \left(\prod_{j=1, j \neq J}^{N+1} \frac{\beta - \beta_j}{\beta_J - \beta_j} \right) \left(\prod_{k=1, k \neq K}^{N+1} \frac{\gamma - \gamma_k}{\gamma_K - \gamma_k} \right). \quad (11)$$

282 Then, any value of the flow variables $V(\alpha, \beta, \gamma)$, such as the wind speed, inside a
 283 hexahedral element can be interpolated from the solutions V_{IJK} , $I, J, K = 1, \dots, N+1$,
 284 on the Legendre-Gauss-Lobatto points as

$$285 \quad V(\alpha, \beta, \gamma) = \sum_{I=1}^{N+1} \sum_{J=1}^{N+1} \sum_{K=1}^{N+1} L_{IJK}(\alpha, \beta, \gamma) V_{IJK}. \quad (12)$$

286 The initial conditions are identical in each model. The hydrostatic and gradient-
 287 wind balanced, tropical storm-like vortex with axisymmetric tangential winds described
 288 in Eq. (10) of Guimond et al. (2016) is utilized here, which is similar to the study of Nolan
 289 and Grasso (2003). The tangential velocity field in the radius–height plane for this ini-
 290 tial vortex is shown in Fig. 1. On top of this vortex, four-dimensional latent heating/cooling
 291 rates derived from airborne Doppler radar measurements in rapidly intensifying Hurri-
 292 cane Guillermo (1997) described in Guimond et al. (2011), are added as a source term
 293 in the potential temperature equation in both WRF and NUMA. These heating fields

294 are computed on a grid covering the inner-core of the system out to a radius of ~ 60 km
 295 with a grid spacing of 2 km and 0.5 km in the horizontal and vertical dimensions, re-
 296 spective. There are ten heating snapshots covering ~ 5.7 h with a time step of ~ 34
 297 minutes. The peak heating is located at a radius of 25 - 30 km, which is well inside the
 298 radius of maximum wind (RMW) of the initial vortex (~ 50 km). This heating and vor-
 299 tex configuration represents the rapid intensification process well, where convective bursts
 300 are the main driving force, e.g., (M. Montgomery et al., 2006; Reasor et al., 2009; Gui-
 301 mond et al., 2010; Rogers et al., 2013). Guimond et al. (2011) conducted an extensive
 302 uncertainty analysis of the latent heat retrievals and found they were reasonably accu-
 303 rate, especially for convective bursts with randomly distributed errors in the heating mag-
 304 nitudes of $\sim 16\%$ for updrafts greater than 5 m/s. In addition, Guimond and Reisner
 305 (2012) inserted the heating retrievals into realistic forecasts of Guillermo and found very
 306 good agreement in the predicted wind fields relative to observations.

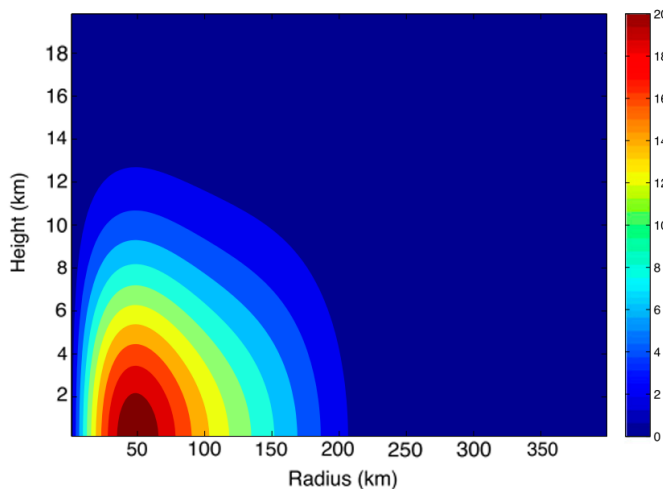


Figure 1: Axisymmetric tangential velocity (m/s) in the radius-height plane for the initial vortex used in each model.

307 Starting from the initial conditions, the first heating snapshot is introduced into
 308 the model over a 30 minute period using a hyperbolic tangent function. Then, the re-
 309 maining heating snapshots are linearly interpolated to the next observation time over
 310 a 34 minute period. After the last observation time, the heating is kept constant up to
 311 6 hours, which is the end of our simulations. Fig. 2 shows the three-dimensional struc-
 312 ture of the heating for three snapshots and the time evolution function used to control
 313 the forcing in the models. Note that we have also added an exponentially decaying func-
 314 tion at the upper-edge of the observational domain (10 km) to smoothly transition the
 315 data into the model grid, which helps maintain numerical stability.

316 Both models are also supplied the same explicit diffusion settings. While we can
 317 utilize the same sub-grid scale turbulence scheme in WRF and NUMA for our compar-
 318 isons, the differences in the dynamic core of each model and associated dissipation char-
 319 acteristics will likely produce different eddy viscosity values during the course of the sim-
 320 ulations. To isolate the model differences to the numerical formulation, we developed a
 321 simple height-dependent eddy viscosity model based on output from the WRF 3D tur-
 322 bulent kinetic energy (TKE) sub-grid turbulence scheme. Initially, we conducted a WRF
 323 simulation with the 3D TKE scheme to get an idea of the eddy viscosity and diffusiv-

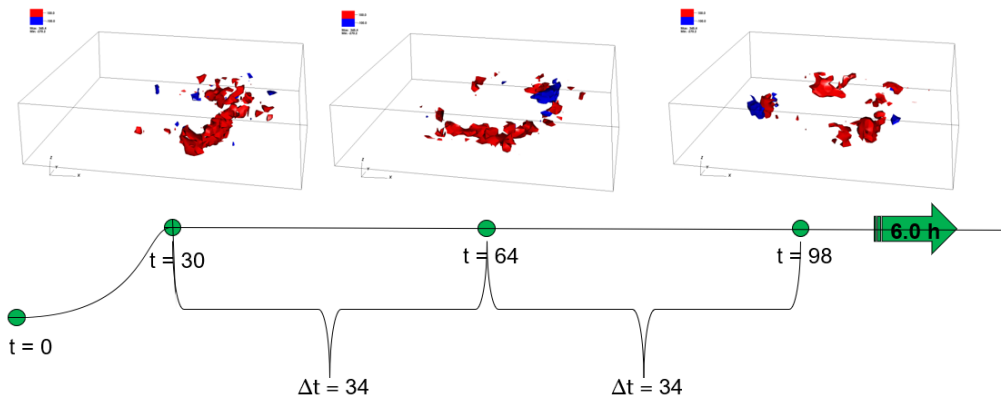


Figure 2: Three-dimensional isosurfaces of latent heating (red; 100 K/h) and cooling (blue; -100 K/h) retrieved from airborne Doppler measurements in rapidly intensifying Hurricane Guillermo (1997). Three example snapshots of this heating are shown with the storm-centered volume extending 120 km on a side in the horizontal and 20 km in the vertical. The time evolution function used to force the heating into the model is also shown with units of minutes, unless noted otherwise.

324 ity values produced from the vortex and heating. Following a parcel, the sources and sinks
 325 of TKE in this scheme depend on the shear, buoyancy and dissipation. Details describ-
 326 ing the implementation of this scheme in WRF, including the parameterization for dis-
 327 sipation, can found in Skamarock et al. (2021). The observational heat forcing will gen-
 328 erate TKE from both the buoyancy and shear terms, but we only focus on the output
 329 eddy viscosities and diffusivities, which are calculated as

$$330 \quad K_{h,v} = C_k l_{h,v} \sqrt{e} \quad (13)$$

331 where e is the TKE, C_k is a constant of 0.15, and l is a length scale, which is around 2000
 332 m in the horizontal and 375 m in the vertical. Figure 3 shows plots of the horizontal eddy
 333 viscosity from the 3D TKE scheme at 0.50 km and 9.80 km height at 6 h . The eyewall
 334 is visible in the figures with viscosity values of $\sim 240\text{ m}^2\text{s}^{-1}$ or larger in a thin ring at
 335 0.5 km height and a broader region of $500 - 750\text{ m}^2\text{s}^{-1}$ values at 9.80 km height.

336 Localized regions of higher viscosity values near $400\text{ m}^2\text{s}^{-1}$ and $1500\text{ m}^2\text{s}^{-1}$ at lower
 337 and upper levels, respectively, are connected to large, vertically coherent heating pulses
 338 from convective bursts. Note that we have set the turbulent Prandtl number in WRF,
 339 which has a default value of $1/3$, to 1 which enables the same eddy viscosity/diffusivity
 340 values for momentum and scalars. There are areas of the WRF software where the de-
 341 fault value is hard coded and we have taken careful steps to maintain values of 1 through-
 342 out the code. The turbulent Prandtl number is set to 1 in NUMA as well.

343 Fig. 4 shows the maximum horizontal and vertical eddy viscosity values produced
 344 over the 6 h WRF simulation as a function of height. Both curves have relatively small
 345 values at lower levels, but they increase sharply at middle levels with some additional
 346 oscillations up to $\sim 16\text{ km}$ height. The large values found at middle to upper levels are
 347 from the strong heating pulses associated with convective bursts as seen in Fig. 3. The
 348 values drop off sharply at $\sim 16\text{ km}$ height because that is where the gravity wave sponge
 349 is introduced into the model. The maximum horizontal viscosity values are about five

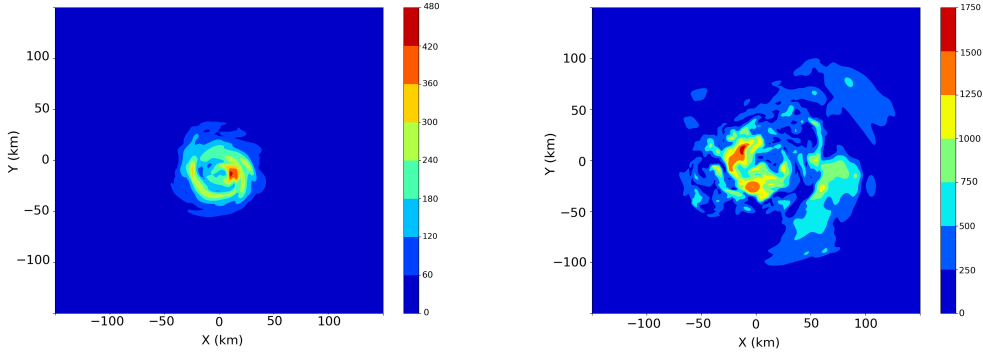


Figure 3: Eddy viscosity values output from the WRF 3D TKE scheme at 6 *h* and 0.5 *km* height (left panel) and 9.8 *km* height (right panel).

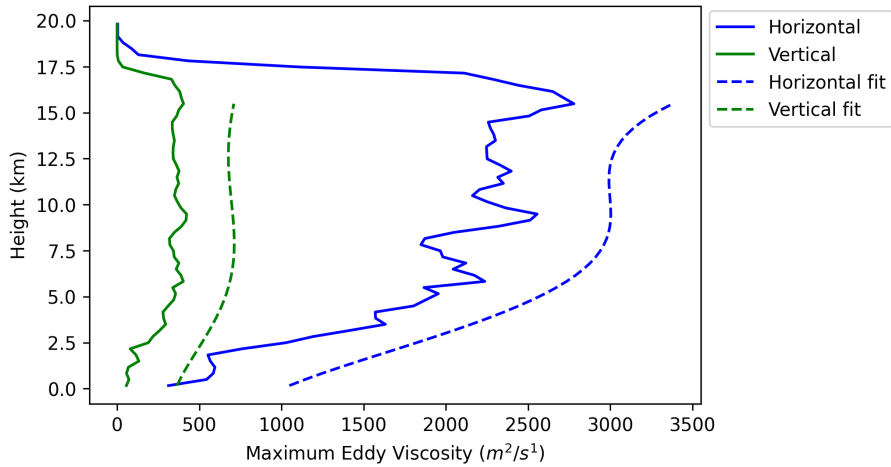


Figure 4: Maximum eddy viscosity values from the 3D TKE scheme in WRF as a function of height. The maximum values are taken over the 6 *h* simulation.

350 times larger than the vertical values. Overlaid on top of the maximum viscosity curves
 351 are high-order polynomial fits that approximate the general structure and values of the
 352 eddy viscosity data. These fits take the following form

$$353 \quad \text{visc}(z) = \tilde{a}z^5 + \tilde{b}z^4 + \tilde{c}z^3 + \tilde{d}z^2 + \tilde{e}z + \tilde{f} \quad (14)$$

354 where z is the geometric height in meters and the coefficients of the fifth-order poly-
 355 nomial are found in Table 1. To stabilize the NUMA code, an extra constant was added
 356 to the \tilde{f} coefficient for both the horizontal and vertical polynomial fits. The \tilde{f} coefficient
 357 is shown in Table 1 and the curves in Fig. 4 include this offset. Finally, these height-dependent
 358 eddy viscosity values are used in *both* WRF and NUMA for momentum and scalar dif-
 359 fusion in the comparison simulations. This simple explicit diffusion model is intended
 360 to both stabilize each numerical model and also represent, to some degree, realistic sub-
 361 grid scale turbulent diffusion from the TKE scheme.

Table 1: Coefficients for the horizontal and vertical viscosity polynomial fits. Both WRF and NUMA use the exact same values.

Coefficients	\tilde{a}	\tilde{b}	\tilde{c}	\tilde{d}	\tilde{e}	\tilde{f}
Horizontal	-0.012760	0.6946	-11.57	53.28	255.90	1003.90
Vertical	-0.004572	0.2150	-3.29	15.05	43.16	357.65

3 Results

3.1 Time Series and Windspeed Structure

In this section, we compare the solutions from the WRF and NUMA control simulations in terms of time series of horizontal wind speed and kinetic energy as well as the structure of windspeed perturbations. Here, perturbation is defined as the total wind speed at a particular time minus the wind speed of the initial condition, which helps identify the wind structures produced from the observational heating.

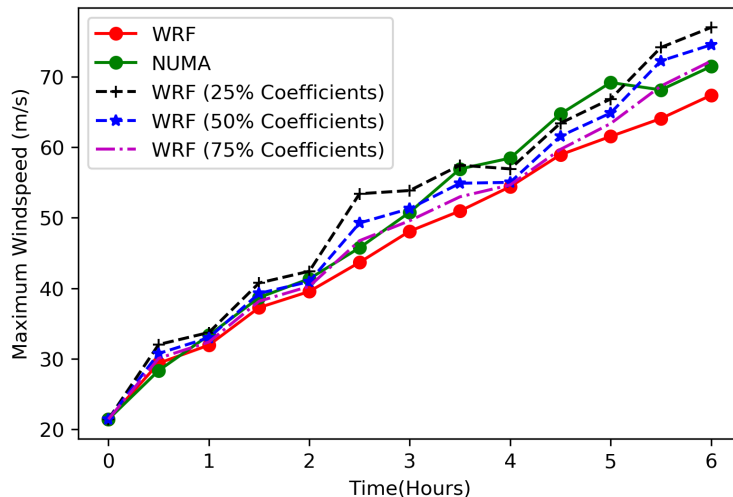


Figure 5: Time series of maximum windspeed for the control WRF and NUMA simulations. The dashed lines show WRF sensitivity tests where the eddy viscosity values were set to a certain percentage of the default values.

Fig. 5 shows the maximum windspeed output every 30 minutes for the control WRF and NUMA simulations with solid red and green lines, respectively. The maximum winds increased by about 45 m/s in 6 h , which is a very large RI rate. The reason for this high rate, besides the idealized setup, is the much larger (and weaker) initial vortex compared to that which occurred in nature, which drives a large inward movement of angular momentum and associated increase in winds. Guimond and Reisner (2012) considered the same observational heating as the present study, but used an initial vortex based on radar observations of Hurricane Guillermo (1997) that had a much smaller RMW ($\sim 30 \text{ km}$) compared to the vortex used here ($\sim 50 \text{ km}$). Guimond and Reisner (2012) found that the minimum pressure dropped by about $12 - 15 \text{ hPa}$ in 6 h with the realistic initial vortex, which compared more favorably with observations than the present vortex. Never-

380 theless, the goal of this study is to analyze the idealized vortex response to heating pulses
 381 derived from observations in a RI system and examine the effects of implicit numerical
 382 dissipation in this process. We do not intend to simulate and reproduce the Guillermo
 383 case study. Thus, the current initial vortex and model setup are sufficient for the goals
 384 of this work.

385 Fig. 5 also shows that after ~ 2 h, the NUMA winds begin to increase relative to
 386 WRF and during the last couple of hours of the simulations, the maximum windspeed
 387 is 2 - 7 m/s or 4 - 12% higher in NUMA compared to WRF. In an attempt to more closely
 388 match the time series of WRF and NUMA, three sensitivity tests were conducted with
 389 WRF where the eddy viscosity values were set to 25%, 50% and 75% of the default val-
 390 ues. The 75% tests still show significantly reduced maximum winds relative to NUMA,
 391 while the 25% tests generally seem too high, especially before 3.5 h. In general, the 50%
 392 tests show a much closer match to NUMA, especially up to and including 3.5 h, despite
 393 the anomalously high value at 2.5 h. There is some larger variability between 4 - 6 h,
 394 but smoothing through that variability indicates a reasonable match to NUMA. There-
 395 fore, these results indicate that in order to produce a similar intensity time series to NUMA,
 396 the explicit diffusion in WRF must be turned down significantly, with a reduction in eddy
 397 viscosity values of $\sim 50\%$ relative to those in NUMA.

398 Additional time series diagnostics for azimuthal mean quantities were also calcu-
 399 lated. While the environment surrounding the vortex has no mean flow, the observational
 400 heat forcing has an azimuthal wavenumber-one structure as can be seen in Fig. 2, which
 401 produces a wavenumber-one flow asymmetry that slowly moves the vortex to the south-
 402 east. The storm center is computed through a simple iterative method that finds the po-
 403 sition which maximizes the azimuthal mean windspeed. The data are interpolated onto
 404 a cylindrical grid with this storm center and the azimuthal mean quantities are calcu-
 405 lated.

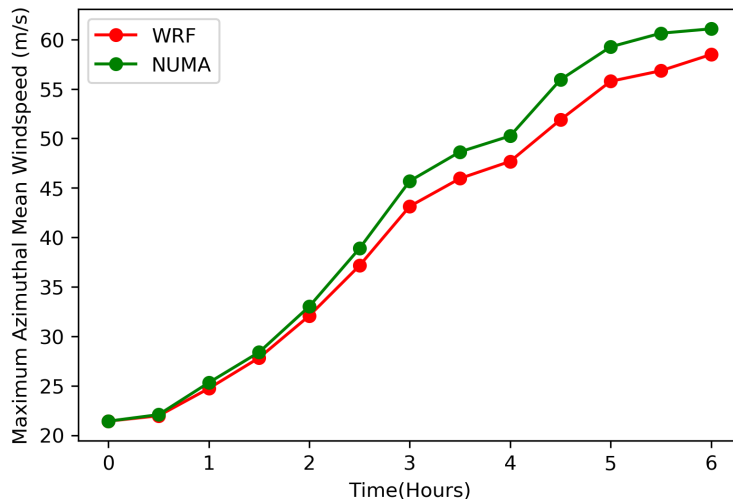


Figure 6: Time series of maximum azimuthal mean windspeed for the control WRF and NUMA simulations.

406 Figs. 6 and 7 show the times series of azimuthal mean windspeed and mean kinetic
 407 energy, respectively. These figures show a similar qualitative pattern as the maximum
 408 windspeed with NUMA producing larger mean windspeeds and kinetic energy values rel-
 409 ative to WRF, with those differences growing over time. In the last couple of hours, the

410 maximum azimuthal mean windspeed is about 4 m/s or 8% higher in NUMA compared
 411 to WRF. The mean kinetic energy follows a very similar pattern to the windspeed and
 412 will be used as a reference for a dynamical budget analysis, presented in Section 3.2, to
 413 explain the reasons behind the model differences. While the differences between WRF
 414 and NUMA are not large for these mean quantities, there is more substantial variability
 415 on local space and time scales, which is demonstrated next. In addition, it is impor-
 416 tant to keep in mind the short time period of these simulations (dictated by the avail-
 417 able observations) and the idealized nature of the setup, both of which will limit the vari-
 418 ability in the models.

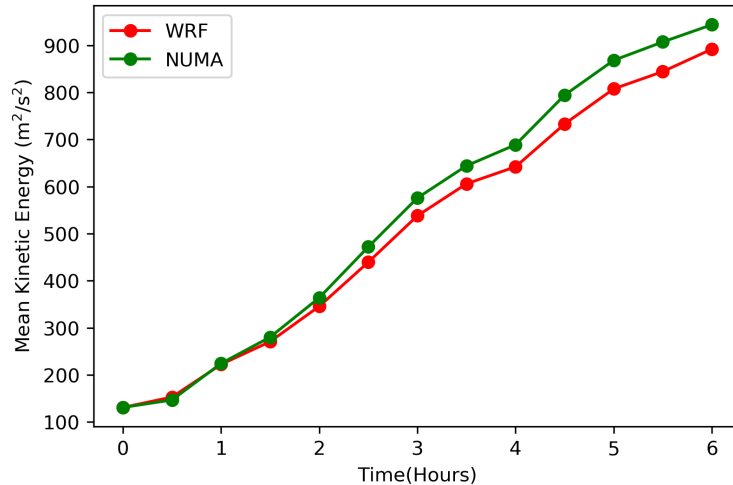


Figure 7: Time series of azimuthal mean kinetic energy averaged over the eyewall ($\sim 10 - 50\text{ km}$ radius) and height ($\sim 0.19 - 1.5\text{ km}$) for the control WRF and NUMA simulations.

419 Snapshots of perturbation wind speed in WRF and NUMA are shown for the 4,
 420 5 and 6 hour time periods in Figs. 8 and 9. At 4 h and 0.19 km height in Fig. 8, the per-
 421 turbation windspeed shows a tight inner-core in both models with the windspeed max-
 422 imum occurring in the North or North-East section of the vortex, reflecting the asym-
 423 metric heating input. The NUMA windspeeds are visibly larger than WRF by about 5
 424 m/s averaged over the eyewall region with peak differences of 6 - 7 m/s in localized re-
 425 gions, such as the larger band in the Eastern eyewall. The majority of the model differ-
 426 ences are concentrated in the center part of the eyewall, but there are also regions
 427 of positive differences in some banded structures to the North and North-East of the cen-
 428 ter. The low wind region in the eye is larger in NUMA when compared to WRF, which
 429 creates a larger radial windspeed gradient when accounting for the larger values in the
 430 eyewall. Outside of the strongest winds in the eyewall and a few banded areas, the model
 431 differences are smaller with some regions positive and other regions negative. At higher
 432 levels (4.83 km height) in Fig. 8, the model differences are smaller with peak positive
 433 values of 4 - 5 m/s in smaller regions. More significant negative values (WRF winds stronger
 434 than NUMA) are occurring at the eye-eyewall interface and also indicate stronger ra-
 435 dial gradients as found at lower levels.

436 At 5 h and 6 h, the vortex has reached peak intensity with perturbation windspeeds
 437 of $\sim 60\text{ m/s}$ found on the Northeast and Northern side of the storm as shown in Fig. 9.
 438 At these time periods, the RMW of the vortex is 15 - 20 km with NUMA on the lower
 439 side and WRF on the higher side of that interval. The RMW of the initial vortex was
 440 $\sim 50\text{ km}$ and this large, rapid contraction rate is consistent with the rapid increase in
 441 winds from conservation of angular momentum.

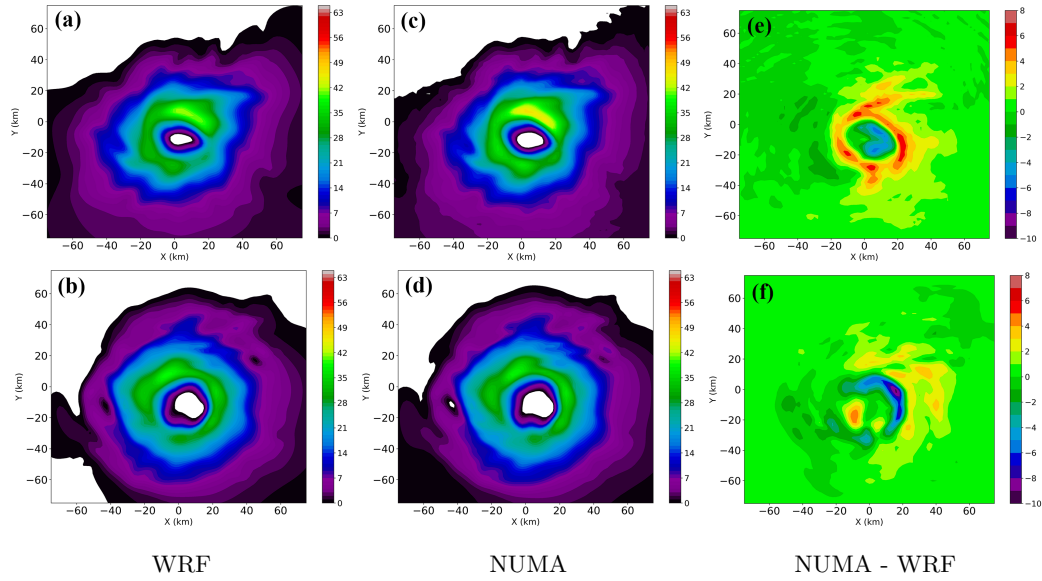


Figure 8: Horizontal wind speed perturbations and differences at 4 h for WRF and NUMA. Panels (a) and (b) show results from WRF at 0.19 km and 4.83 km heights, respectively, while panels (c) and (d) show results from NUMA at the same levels. Panels (e) and (f) show the differences (NUMA - WRF) at the same heights.

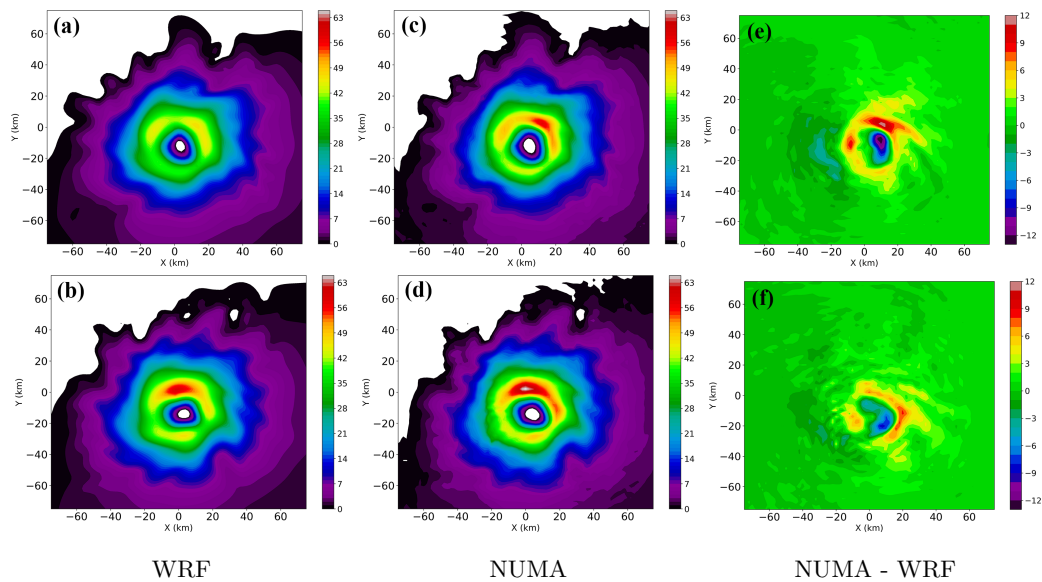


Figure 9: The same as in Fig. 8, only showing the 0.19 km height level at 5 h and 6 h in WRF in panels (a) and (b), respectively and NUMA in panels (c) and (d). Panels (e) and (f) show the differences (NUMA - WRF) at the same corresponding time periods.

At 5 *h*, NUMA shows significantly stronger winds than WRF by 7 - 8 *m/s* within large portions of the northern eyewall including peak differences of up to +12 *m/s*. Similar to the previous time period, the low-wind eye of NUMA is a bit wider than WRF, which produces large negative differences in the eye and a larger radial wind gradient. Some thin bands of higher wind differences can also be seen to the North and Northeast of the storm, which may be related to vortex Rossby wave dynamics. At 6 *h*, the local wind differences are smaller, but still significant in that much of the eyewall has positive differences of ~ 5 *m/s* with larger values on the Eastern side of the vortex.

3.2 Budget Analyses

The previous section established clear differences between the two numerical models with NUMA producing a larger intensity response. How can this be given that each model was set up exactly the same with the same initial conditions and same heat forcing? The answer to this question lies in the design of the numerical schemes that make up the dynamic core of each model and in this section, we analyze how the intensity differences are produced and highlight parts of the numerical scheme that are driving this effect.

The horizontal kinetic energy for the azimuthal mean vortex in cylindrical coordinates (r, θ, z) is expressed as

$$\bar{K} = \frac{1}{2}(\bar{u}^2 + \bar{v}^2) \quad (15)$$

where u is the radial windspeed, v is the tangential windspeed and the overbar indicates an azimuthal mean quantity. After azimuthally averaging, these variables and those below are functions of radius (r) and height (z) unless noted otherwise. After multiplying the radial and tangential equations of motion by their corresponding velocity, summing the two equations and applying Reynolds decomposition in the azimuthal direction (the over bar and prime notations below indicate azimuthal mean and eddy variables, respectively), we arrive at the transport equation for azimuthal mean kinetic energy,

$$\frac{\partial \bar{K}}{\partial t} = M + E + P + D \quad (16)$$

where,

$$M = - \left(\frac{1}{r} \frac{\partial}{\partial r} (\bar{u} \bar{K} r) + \frac{1}{\bar{\rho}} \frac{\partial}{\partial z} (\bar{w} \bar{K} \bar{\rho}) \right),$$

$$E = - \left(\frac{\bar{u}}{r} \frac{\partial}{\partial r} (\overline{u'u'r}) + \frac{\bar{u}}{\bar{\rho}} \frac{\partial}{\partial z} (\overline{u'w'\bar{\rho}}) + \frac{\bar{v}}{\bar{\rho}} \frac{\partial}{\partial z} (\overline{v'w'\bar{\rho}}) + \frac{\bar{v}}{r} \frac{\partial}{\partial r} (\overline{u'v'r}) - \frac{\overline{uv'v'}}{r} + \frac{\overline{vu'v'}}{r} \right),$$

$$P = - \frac{\bar{u}}{\bar{\rho}} \left(\frac{\partial \bar{p}}{\partial r} \right), \quad \text{and} \quad D = (\bar{u} \bar{D}_r + \bar{v} \bar{D}_\theta).$$

In Eq. (16), M defines the mean kinetic energy transport terms, E defines the eddy transport terms which represent the Reynolds stress contributions in the azimuthal dimension, P defines the pressure gradient term and D defines the total explicit diffusion term.

Fig. 10 shows a times series of azimuthal mean kinetic energy budget tendencies from both WRF and NUMA after averaging the fields over the eyewall ($\sim 10 - 50$ *km* radius) and height ($\sim 0.19 - 1.5$ *km*). The largest term is the pressure gradient, which contributes positively to the increase in mean kinetic energy of the vortex shown in Fig. 7. This large positive contribution is from the input heating, which leads to significant integrated warming in the storm core and an associated increase in the radial pressure gradient between the undisturbed outer regions and lowered pressures in the core region.

486 This larger radial pressure gradient drives strong inflow at low levels, which transports
 487 high angular momentum from the outer regions of the storm towards the center, increas-
 488 ing the tangential velocity of the vortex. Large differences between WRF and NUMA
 489 are present in the pressure gradient term, especially beyond 2 h with NUMA larger than
 490 WRF by $\sim 25\%$ on average with a maximum of $\sim 40\%$.

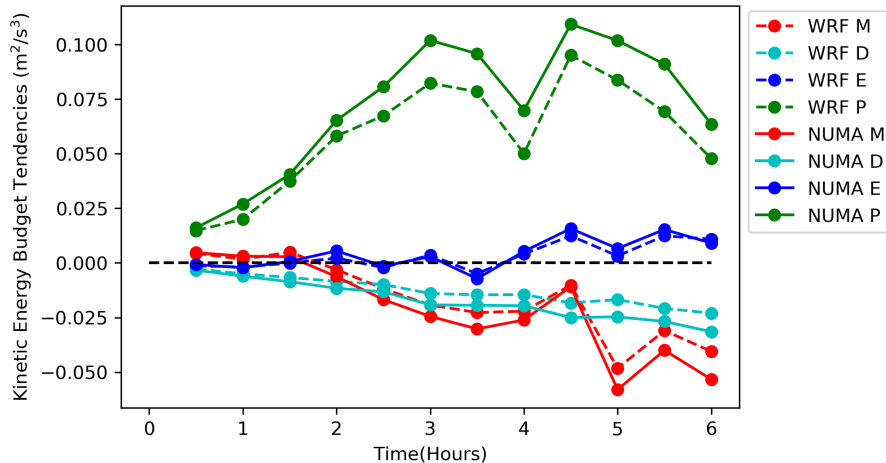


Figure 10: Time series of azimuthal mean kinetic energy budget tendencies from both models after averaging the fields over the eyewall ($\sim 10 - 50 \text{ km}$ radius) and height ($\sim 0.19 - 1.5 \text{ km}$). The black dashed line highlights zero tendency and all other lines are denoted in the key.

491 The second largest contribution is the mean transport term, which shows largely
 492 negative values that increase with time as the mean flow intensifies. The vertical mean
 493 transport dominates over the horizontal transport, which is dictated by the heating pro-
 494 file that is maximized near middle levels. Therefore, there is a significant positive flux
 495 of kinetic energy out of the lower levels of the vortex, which results in a net sink of en-
 496 ergy. However, the differences between WRF and NUMA are much smaller for the mean
 497 transport term, relative to the pressure gradient, by a factor of ~ 4.5 . The eddy trans-
 498 port term oscillates around zero tendency up until $\sim 3.5 \text{ h}$ after which a clear positive
 499 contribution to the mean kinetic energy is visible. After summing all the budget terms,
 500 the eddy transport contributes up to 15 - 40% to the increase in mean KE of the vor-
 501 tex over the 6 h period. When integrating the budget terms over time, the eddy trans-
 502 port contributes 18% to the mean kinetic energy with no notable differences between the
 503 models. At these later time periods, the vertical divergence of the vertical tangential mo-
 504 mentum flux (the third term in the E contribution in Eq. (16)) has the largest values
 505 and provides a positive tendency to the mean kinetic energy in our analysis domain.

506 For the total explicit diffusion term, the values are very similar before $\sim 1 \text{ h}$, but
 507 after that time the values from NUMA start to slowly increase relative to WRF with con-
 508 sequential differences at later times into the simulation (NUMA larger than WRF by \sim
 509 36% when averaged from 2 - 6 h). The reason for this is that while the eddy viscosity
 510 values are fixed, the velocity gradients in NUMA are larger than WRF (described in the
 511 previous section), which produces a larger magnitude in the Laplacian operator. This
 512 is not a truly fair comparison of the dynamic cores and a simple diagnostic calculation
 513 that accounts for this effect is outlined below.

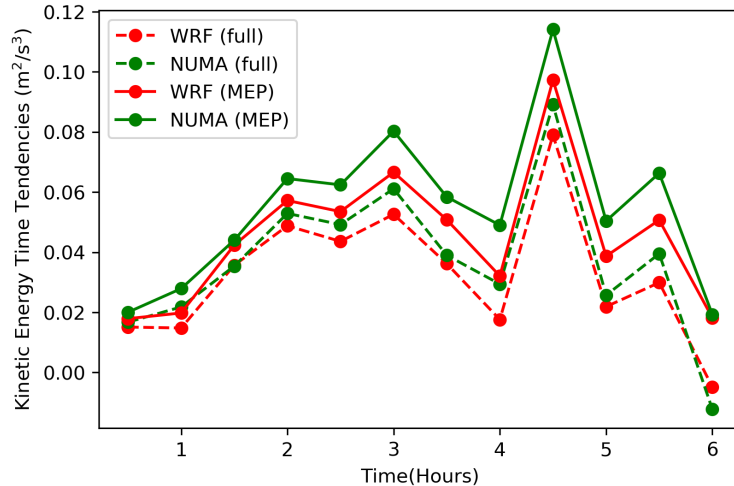


Figure 11: Time series of the summation of terms that control the time tendency of azimuthal mean kinetic energy on the RHS of Eqn (16). The dashed lines represent all terms on the RHS of Eq. (16), while the solid lines include only the M , E and P terms. After summation, the fields are averaged over the eyewall ($\sim 10 - 50 \text{ km}$ radius) and height ($\sim 0.19 - 1.5 \text{ km}$) as is done in Fig. 10.

514 Fig. 11 shows a times series of the summation of all terms on the RHS of Eq. (16)
 515 for WRF and NUMA (dashed lines). This figure represents the slope of the curves displayed
 516 in the time series of mean kinetic energy in Fig. 7. Clearly, there is intensification
 517 throughout the simulation with the exception of the last output time at 6 h , but
 518 note that this weakening is not shown in Fig. 7 because the last output time is right at
 519 6 h . The intensification rate hovers between $0.03 - 0.05 \text{ m}^2/\text{s}^3$ over most of the simu-
 520 lation with the exception of a large spike at 4.5 h . After integrating these time series curves
 521 with the trapezoidal rule over 6 h with the 30-minute output interval, we find that NUMA
 522 has a larger mean (azimuthal mean and averaged over $r = 10 - 50 \text{ km}$ and $z = 0.19 -$
 523 1.5 km) kinetic energy than WRF by $\sim 8\%$. However, this difference does not account
 524 for the larger explicit diffusion in NUMA mentioned above, which obscures the ability
 525 to isolate the effects of implicit numerical dissipation. To correct for this, we re-calculated
 526 the integrated mean kinetic energy with the explicit diffusion term (D) removed and we
 527 find that NUMA has larger values than WRF by $\sim 18\%$. Note that the same percent-
 528 age difference would be found if we used the exact same explicit diffusion term from ei-
 529 ther WRF or NUMA (see Fig. 10) in each model. However, there is a coupled, nonlin-
 530 ear evolution of the fields whereby differences in the explicit diffusion affect the other
 531 terms in the mean kinetic energy during the simulations. This is difficult to control, and
 532 we do not address this issue here.

533 In summary, the main differences in the mean vortex intensity between WRF and
 534 NUMA is due to the radial pressure gradient contribution to the mean kinetic energy
 535 with smaller effects from the transport terms and explicit diffusion. However, even the
 536 transport and explicit diffusion terms are controlled, for the most part, by the pressure
 537 gradient term because the differences in each model's response to the input heating, via
 538 the pressure gradient, results in different velocities even very early (e.g., 1 h) into the
 539 simulations (see Fig. 10). Thus, differences in the calculation of the nonlinear advective
 540 terms in each model is not a significant source of diffusion and this result is consistent
 541 with Guimond et al. (2016). In addition, this result follows from the fact that both WRF

542 and NUMA utilize high-order discretization of the advective terms and WRF showed no
543 tangible differences when switching from the 5th order to 6th order stencil.

544 Guimond et al. (2016) also identified the pressure gradient term as the controlling
545 factor in dynamic core comparisons between three different models (including WRF and
546 NUMA) for the same vortex analyzed here. However, Guimond et al. (2016) only con-
547 sidered idealized potential temperature perturbations to the initial state of the model
548 as opposed to the time-dependent, 3-D observational heating used here. Guimond et al.
549 (2016) conducted sensitivity tests with different order time integration schemes and found
550 significant differences in the solutions, which led to the conclusion that the diffusion in
551 WRF was due to the temporal discretization. Similar sensitivity tests were conducted
552 in this work by comparing the control NUMA run (essentially a first-order in time method)
553 to a second-order in time Runge-Kutta method, which is very similar to WRF. These
554 sensitivity tests in NUMA revealed small differences with peak absolute values of ~ 1.5
555 m/s (not shown) indicating that the temporal discretization is *not* significantly affect-
556 ing the solutions in either NUMA or WRF. For the spatial discretization of the pressure
557 gradient term, WRF uses second-order finite differences while NUMA is utilizing 5th-
558 order polynomials, which also provides fifth-order accuracy for the pressure gradient eval-
559 uation. Given the kinetic energy budgets and sensitivity tests described above, we as-
560 sess that the low-order spatial approximation of the pressure gradient term in WRF is
561 the source of the significant diffusion in the vortex intensity identified in this paper.

Given the large model differences in the pressure gradient contribution to the mean
kinetic energy demonstrated in Fig. 10, it is imperative to examine the full structure of
this term to identify any potential localized signals. The components of the horizontal
pressure gradient contribution to the kinetic energy in cylindrical coordinates are given
as

$$\frac{-u}{\rho} \frac{\partial \hat{p}}{\partial r} \quad \text{and} \quad \frac{-v}{\rho} \frac{\partial \hat{p}}{\partial \theta}$$

562 where u and v are the radial and tangential wind speed, respectively. Figs. 12 and 13
563 show horizontal cross sections of these terms, averaged over low-levels ($\sim 0.19 - 1.5$ km),
564 at 4 h and 5 h into the simulations, respectively. In addition, select height-averaged (over
565 the full column) heating inputs to the models leading up to these time periods are also
566 shown in Figs. 12 and 13.

567 Figs. 12a, 12b show the heating inputs at 3.33 h , 4 h , which represent the heating
568 snapshots leading up to the 4 h mark in the simulations. The 4 h heating has the larger
569 weight in the model results, but there is still some “memory” of the heating from ear-
570 lier times. The radial component of the pressure term in WRF (Fig. 12c) and NUMA
571 (Fig. 12e) shows an azimuthal wavenumber-2 structure in the eyewall region, which is
572 connected to the input heating structure most closely at 4 h . The heating at 4 h shows
573 localized regions of large positive and negative heating rates (see, for example, the fea-
574 ture to the West of the storm center in Fig. 12b), which are correlated with the positive/negative
575 couplet in the radial pressure term in a similar region. Note that due to the vortex drift
576 to the South-East over time, the heating input and radial pressure term are not exactly
577 aligned. Comparing the radial pressure term from WRF and NUMA shows that NUMA
578 has larger values than WRF, especially in the localized positive regions. This is the rea-
579 son why the azimuthal average of these fields (see Fig. 10) shows NUMA with much larger
580 values than WRF. *This result indicates that strong, localized heating regions associated*
581 *with convective bursts are producing a concomitant, enhanced pressure gradient response*
582 *in NUMA that is driving the differences in the intensification of the vortex.* The reduced,
583 localized pressure gradient values in WRF are due to diffusion from the low-order spa-
584 tial discretization of this term, as described above.

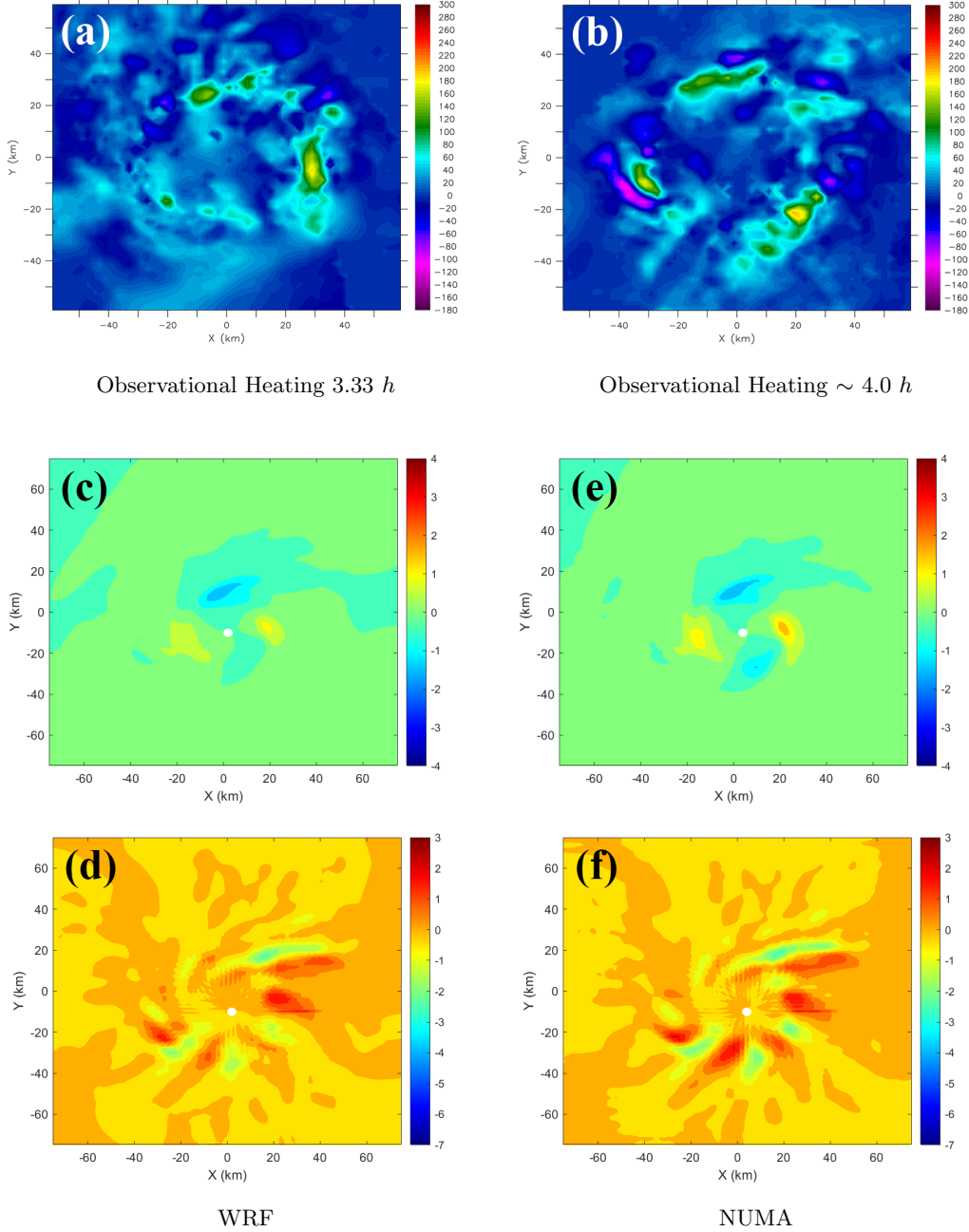


Figure 12: Panels (a) and (b) show the height-averaged, observational heating inputs to the models for time periods 3.33 h and $\sim 4 h$, respectively. Panels (c) and (d) show the horizontal pressure gradient contributions to kinetic energy in WRF for the radial and tangential components, respectively. Panels (e) and (f) are the same as in (c) and (d), only for NUMA. Panels (c) - (f) are at 4 h into the simulations.

585 The azimuthal component of the pressure term for this time period in both WRF
 586 (Fig. 12d) and NUMA (Fig. 12f) shows a clear azimuthal wave structure with an average
 587 wavelength of $\sim 20 km$ and \sim wavenumber-5 structure. These waves are very likely
 588 convectively forced vortex Rossby waves (M. T. Montgomery & Enagonio, 1998), but are

589 not discussed in detail. The anticipated vortex Rossby waves in NUMA have a larger
 590 amplitude than those in WRF and this can be seen most clearly to the south of the vor-
 591 tex center.

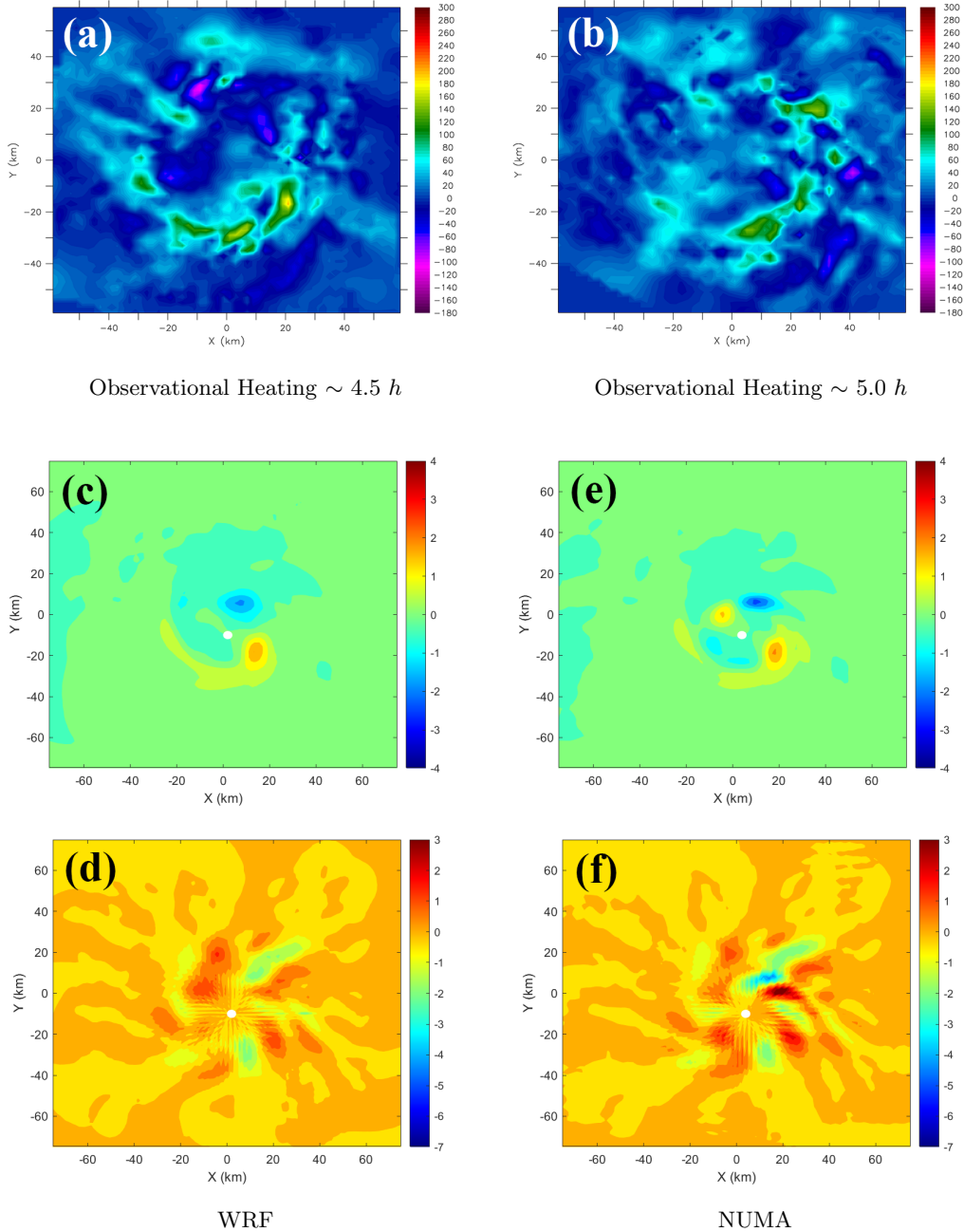


Figure 13: Panels (a) and (b) show the height-averaged, observational heating inputs to the models for time periods $\sim 4.5 h$ and $\sim 5.0 h$, respectively. All other panels are the same as in Figure 12, only for 5 h into the simulations.

592 Fig. 13 shows the same fields as Fig. 12, only at 5 *h* into the simulations. Similar
 593 results to those at 4 *h* are observed, including larger magnitude, localized positive anom-
 594 alies in the radial pressure term in NUMA (Fig. 12e) compared to WRF (Fig. 12c) that
 595 are connected to the heating snapshots at this time (Figs. 13a and 13b). The azimuthal
 596 pressure term also continues to show evidence of vortex Rossby waves with clearly larger
 597 amplitude features to the North and East of the vortex center. The heating input at 5
 598 *h* (Fig. 13b) shows that the majority of the heating is on the eastern side of the vortex
 599 with large, localized regions to the north-east of the center, which is consistent with the
 600 larger amplitude waves in NUMA.

601 4 Summary and Conclusions

602 In this paper, we have studied the computational fluid dynamics of the hurricane
 603 rapid intensification (RI) process by considering idealized simulations of the vortex re-
 604 sponse to time-dependent, 3D latent heating estimates derived from airborne radar mea-
 605 surements collected in the RI of Hurricane Guillermo (1997). Two types of numerical
 606 models were considered: a community-based, finite difference and split-explicit model
 607 called WRF and an advanced, spectral element and semi-implicit model called NUMA.
 608 The models are carefully analyzed and setup to ensure the differences can be isolated
 609 to the numerical schemes that comprise the dynamic core. This includes explicit diffu-
 610 sion settings, which are parameterized based on output from a 3D TKE subgrid model
 611 experiment.

612 Prior studies used simple thermal perturbations to the initial conditions to repre-
 613 sent the effects of convective heating and found that the WRF model had significant im-
 614 plicit numerical dissipation when compared to advanced research codes, including NUMA
 615 (Guimond et al., 2016). The current study also finds significant implicit numerical dis-
 616 sipation in WRF with a reduction in several intensity metrics over a 6 *h* period: (1) max-
 617 imum wind speeds in WRF are $\sim 12\%$ lower than NUMA when matching the eddy dif-
 618 fusivity values, (2) time-integrated, mean kinetic energy values in WRF are $\sim 20\%$ lower
 619 than NUMA when accounting for differences in the Laplacian diffusion operator and (3)
 620 peak, localized wind speed differences in WRF are ~ 12 *m/s* lower than NUMA. Sen-
 621 sitivity studies show, that in order to achieve a similar intensity time series to NUMA,
 622 the explicit diffusion in WRF must be reduced drastically, with eddy viscosity values set
 623 to 50% of those in NUMA. In the control simulations, the NUMA windspeeds are vis-
 624 ibly larger than WRF by roughly 5 *m/s* when averaged over the eyewall with local re-
 625 gions exceeding 10 *m/s*. In addition, NUMA's low wind region in the eye is slightly wider
 626 than WRF's, resulting in larger velocity gradients (and larger Laplacian diffusion) when
 627 accounting for the enhanced values in the eyewall.

628 To understand the nature of the differences between the models, the azimuthal mean
 629 kinetic energy budget was examined. At all time periods in the 6-hour simulation, the
 630 pressure gradient force contribution to the kinetic energy is significantly higher in NUMA
 631 compared to WRF by $\sim 23\%$ in the mean and $\sim 40\%$ in the maximum. Examination
 632 of the horizontal components of the pressure term reveal that NUMA produces localized
 633 pressure gradient anomalies that are larger in magnitude when compared to WRF. These
 634 localized regions are tied into the observational heating inputs that contain the presence
 635 of convective bursts, which are prevalent during the RI process. In addition, the pres-
 636 ence of azimuthal waves in the pressure gradient term are visible in the simulations, likely
 637 vortex Rossby waves, with larger amplitudes in NUMA. While the axisymmetric trans-
 638 port of kinetic energy, especially by vertical fluxes, is substantially larger than the asym-
 639 metric transport, we find that these eddy processes contribute 15 - 40% at 30-minute out-
 640 put intervals over the 6 *h* period and $\sim 18\%$ when integrating the terms over time.

641 Sensitivity tests with different time integration schemes in NUMA were conducted
 642 to identify the root numerical causes of the model differences. However, employing a second-

643 order in time scheme, compared to an essentially first-order in time method for the con-
 644 trol run, did not produce any notable differences in the NUMA solutions. This is in con-
 645 trast to the results in Guimond et al. (2016), where higher order time integration schemes
 646 produced even more energetic solutions. The reason for the discrepancy is likely due to
 647 the nature of the problem: Guimond et al. (2016) analyzed a freely evolving vortex ini-
 648 tialized with a perturbation while the present study considered strong, 4-D forcing. There-
 649 fore, the significant diffusion in WRF is controlled by a spatial discretization error and
 650 this is consistent with the fact that WRF relies on a diffusive, second-order approxima-
 651 tion to the pressure gradient force while NUMA utilized a fifth-order accurate approx-
 652 imation.

653 We do not know which model solution is correct in the absolute sense and numer-
 654 ical convergence studies are ongoing. However, excessive numerical dissipation is not a
 655 desired aspect of a modeling system because it reduces the effective resolution of the sim-
 656 ulations and can damage the effects of physics-based sub-grid models and observations
 657 used to initialize the model in data assimilation practices. The simulations in this pa-
 658 per were for a short time period (6 h) to accommodate the available observational heat-
 659 ing and longer-term simulations that have multiple, episodic convective burst events will
 660 likely increase the disparity between the two dynamic cores. Furthermore, the positive
 661 feedback loop involving moist physics was not operating in these simulations and cou-
 662 pling of the enhanced windspeeds in NUMA to surface fluxes, microphysical heating and
 663 pressure responses will likely add additional divergence in the models. Nevertheless, this
 664 paper makes an important step forward in an attempt to develop a holistic, thorough
 665 investigation of the computational fluid dynamics of the hurricane RI process.

666 Acknowledgments

667 We thank NOAA/HRD for collecting and processing the raw radar data used in this pa-
 668 per. The hardware used for the computational studies in this paper is part of the Uni-
 669 versity of Maryland, Baltimore County (UMBC) High Performance Computing Facil-
 670 ity (HPCF). HPCF is supported by the U.S. National Science Foundation through the
 671 MRI program (grant nos. CNS-0821258, CNS-1228778, and OAC-1726023) and the SCREMS
 672 program (grant no. DMS-0821311), with additional substantial support from UMBC.
 673 The contributions of M.B. Hasan and S.R. Guimond are partially supported by the NSF
 674 under grant AGS-2121366. Additional support for M.B. Hasan was provided by a UMBC
 675 Strategic Awards for Research Transitions (START) grant to S.R. Guimond. S. Reddy
 676 and F.X. Giraldo were supported by the Office of Naval Research under grant number
 677 N0001419WX00721.

678 The WRF and NUMA output data are available at the following link: [https://
 679 figshare.com/projects/The_Effects_of_Numerical_Dissipation_on_Hurricane_Rapid
 680 _Intensification_with_Observational_Heating/126469](https://figshare.com/projects/The_Effects_of_Numerical_Dissipation_on_Hurricane_Rapid_Intensification_with_Observational_Heating/126469).

681 References

- 682 Abdi, D., Giraldo, F. X., Constantinescu, E. M., Carr, L. E., Wilcox, L. C., & War-
 683 burton, T. C. (2019). Acceleration of the implicit–explicit nonhydrostatic
 684 unified model of the atmosphere on manycore processors. *The Interna-
 685 tional Journal of High Performance Computing Applications*, 33(2), 242-
 686 267. Retrieved from <https://doi.org/10.1177/1094342017732395> doi:
 687 10.1177/1094342017732395
- 688 Abdi, D., Wilcox, L., Warburton, T., & Giraldo, F. X. (2017). A gpu-accelerated
 689 continuous and discontinuous galerkin non-hydrostatic atmospheric model. *The
 690 International Journal of High Performance Computing Applications*, 33(1),
 691 81-109. Retrieved from <https://doi.org/10.1177/1094342017694427> doi:

- 692 10.1177/1094342017694427
693 Blaisdell, G., Spyropoulos, E., & Qin, J. (1996). The effect of the formulation of
694 nonlinear terms on aliasing errors in spectral methods. *Applied Numerical*
695 *Mathematics*, *21*, 207–219.
- 696 Cockburn, B., & Shu, C.-W. (1998). The runge–kutta discontinuous galerkin method
697 for conservation laws v: Multidimensional systems. *Journal of Computational*
698 *Physics*, *141*(2), 199–224.
- 699 DeMaria, M., Franklin, J. L., Onderlinde, M. J., & Kaplan, J. (2021). Opera-
700 tional forecasting of tropical cyclone rapid intensification at the national hur-
701 ricane center. *Atmosphere*, *12*(6). Retrieved from [https://www.mdpi.com/](https://www.mdpi.com/2073-4433/12/6/683)
702 [2073-4433/12/6/683](https://www.mdpi.com/2073-4433/12/6/683) doi: 10.3390/atmos12060683
- 703 DeMaria, M., Sampson, C., Knaff, J., & Musgrave, K. D. (2014). Is tropical cyclone
704 intensity guidance improving. *Bulletin of the American Meteorological Society*,
705 *95*, 387–398.
- 706 Emanuel, K. (1986). An air-sea interaction theory for tropical cyclones. Part I:
707 Steady-state maintenance. *JAS*, *43*, 585–604.
- 708 Fischer, P. F., & Mullen, J. S. (2001). Filter-based stabilization of spectral element
709 methods. *Comptes Rendus de l'Académie des Sciences - Series I - Mathemat-*
710 *ics*, *332*, 265–270.
- 711 Gassner, G. J. (2013). A skew-symmetric discontinuous galerkin spectral element
712 discretization and its relation to sbp-sat finite difference methods. *SIAM Jour-*
713 *nal on Scientific Computing*, *35*, A1233–A1253.
- 714 Gassner, G. J., & Beck, A. D. (2013). On the accuracy of high-order discretizations
715 for underresolved turbulence simulations. *Theor. Comput. Fluid Dyn.*, *27*,
716 221–237.
- 717 Giraldo, F. X. (2020). *An introduction to element-based galerkin methods on tensor-*
718 *product bases: Analysis, algorithms, and applications*. doi: 10.1007/978-3-030
719 -55069-1
- 720 Giraldo, F. X., Kelly, J. F., & Constantinescu, E. M. (2013). Implicit-explicit formu-
721 lations of a three-dimensional nonhydrostatic unified model of the atmosphere
722 (numa). *SIAM J. Sci. Comput.*, *35*.
- 723 Giraldo, F. X., & Restelli, M. (2008). A study of spectral element and discontinuous
724 Galerkin methods for the Navier Stokes equations in nonhydrostatic mesoscale
725 atmospheric modeling: Equation sets and test cases. *Journal of Computational*
726 *Physics*, *227*(8), 3849–3877. doi: 10.1016/j.jcp.2007.12.009
- 727 Giraldo, F. X., Restelli, M., & Läuter, M. (2010). Semi-implicit formulations of the
728 navier–stokes equations: Application to nonhydrostatic atmospheric modeling.
729 *SIAM J. Sci. Comput.*, *32*, 3394–3425.
- 730 Guimond, S. R., Bourassa, M., & Reasor, P. (2011). A Latent Heat Retrieval and Its
731 Effects on the Intensity and Structure Change of Hurricane Guillermo (1997).
732 Part I: The Algorithm and Observations. *Journal of The Atmospheric Sciences*
733 *- J ATMOS SCI*, *68*, 1549–1567. doi: 10.1175/2011JAS3700.1
- 734 Guimond, S. R., Heymsfield, G. M., & Turk, F. J. (2010). Multiscale observations of
735 Hurricane Dennis (2005): The effects of hot towers on rapid intensification. *J.*
736 *Atmos. Sci.*, *67*.
- 737 Guimond, S. R., Reisner, J., Marras, S., & Giraldo, F. X. (2016). The impacts of
738 dry dynamic cores on asymmetric hurricane intensification. *Journal of the At-*
739 *mospheric Sciences*, *73*, 4661 - 4684. doi: 10.1175/JAS-D-16-0055.1
- 740 Guimond, S. R., & Reisner, J. M. (2012). A latent heat retrieval and its effects on
741 the intensity and structure change of Hurricane Guillermo (1997). *Part II: Nu-*
742 *merical simulations*. *J. Atmos. Sci.*, *69*.
- 743 Hoffman, J., & Frankel, S. (2001). *Numerical methods for engineers and scientists,*
744 *second edition*,. Taylor & Francis. Retrieved from [https://books.google](https://books.google.com/books?id=VKs7Afjkng4C)
745 [.com/books?id=VKs7Afjkng4C](https://books?id=VKs7Afjkng4C)
- 746 Honein, A. E., & Moin, P. (2004). Higher entropy conservation and numerical stabil-

- ity of compressible turbulence simulations. *Journal of Computational Physics*, 201(2), 531–545. Retrieved from <https://www.sciencedirect.com/science/article/pii/S0021999104002414> doi: <https://doi.org/10.1016/j.jcp.2004.06.006>
- Karamanos, G.-S., & Karniadakis, G. (2000). A spectral vanishing viscosity method for large-eddy simulations. *Journal of Computational Physics*, 163, 22–50.
- Kelly, J. F., & Giraldo, F. X. (2012). Continuous and discontinuous Galerkin methods for a scalable three-dimensional nonhydrostatic atmospheric model: limited-area mode [Article]. *Journal of Computational Physics*, 231(24), 7988–8008. doi: {10.1016/j.jcp.2012.04.042}
- Klemp, J., & Wilhelmson, R. (1978). The simulation of three-dimensional convective storm dynamics. *J. Atmos. Sci.*, 35, 1070–1096. doi: 10.1175/1520-0469(1978)035<1070:TSOTDC>2.0.CO;2
- Knutson, T., Camargo, S., Chan, J., Kerry, E., Chang-Hoi, H., James, K., ... Liguang, W. (2019). Tropical cyclones and climate change assessment: part II. Projected Response to Anthropogenic Warming. *Bull. Am. Meteorol. Soc.*, 101, E303–E322.
- Knutson, T., Sirutis, J., Zhao, M., Tuleya, R., Bender, M., Vecchi, G., ... Chavas, D. (2015). Global projections of intense tropical cyclone activity for the late twenty-first century from dynamical downscaling of downscaling of CMIP5/RCP4.5 scenarios. *J. Climate*, 28, 7203–7224.
- Kravchenko, A., & Moin, P. (1997). On the effect of numerical errors in large eddy simulations of turbulent flows. *Journal of Computational Physics*, 131(2), 310–322. Retrieved from <https://www.sciencedirect.com/science/article/pii/S0021999196955977> doi: <https://doi.org/10.1006/jcph.1996.5597>
- Laprise, R. (1992). The euler equations of motion with hydrostatic pressure as an independent variable. *Monthly Weather Review - MON WEATHER REV*, 120. doi: 10.1175/1520-0493(1992)120<0197:TEEOMW>2.0.CO;2
- Larsson, J., Lele, S., & Moin, P. (2007). Effect of numerical dissipation on the predicted spectra for compressible turbulence. *Annual research briefs*.
- Li, L., & Chakraborty, P. (2020). Slower decay of landfalling hurricanes in a warming world. *Nature*, 587(7833), 230–234. Retrieved from <https://doi.org/10.1038/s41586-020-2867-7> doi: 10.1038/s41586-020-2867-7
- Marks, F., & Shay, L. (1998). Landfalling tropical cyclones: Forecast problems and associated research opportunities. *Bulletin of the American Meteorological Society*, 79, 305–323.
- Montgomery, M., Nicholls, M., Cram, T., & Saunders, A. (2006). A vortical hot tower route to tropical cyclogenesis. *Journal of the atmospheric sciences*, 63(1), 355–386.
- Montgomery, M. T., & Enagonio, J. (1998). Tropical cyclogenesis via convectively forced vortex rossby waves in a three-dimensional quasigeostrophic model. *Journal of the Atmospheric Sciences*, 55(20), 3176 - 3207. Retrieved from https://journals.ametsoc.org/view/journals/atsc/55/20/1520-0469_1998_055_3176_tcvcfv_2.0.co_2.xml doi: 10.1175/1520-0469(1998)055<3176:TCVCFV>2.0.CO;2
- Moura, R., Mengaldo, G., Peiró, J., & Sherwin, S. (2017). On the eddy-resolving capability of high-order discontinuous Galerkin approaches to implicit LES / under-resolved DNS of euler turbulence. *Journal of Computational Physics*, 330, 615–623. Retrieved from <https://www.sciencedirect.com/science/article/pii/S0021999116305642> doi: <https://doi.org/10.1016/j.jcp.2016.10.056>
- Nolan, D. S., & Grasso, L. D. (2003). Nonhydrostatic, three-dimensional perturbations to balanced, hurricane-like vortices. part ii: Symmetric response and nonlinear simulations. *JAS*, 60(22), 2717–2745.
- Persson, P.-O., & Peraire, J. (2006). Sub-cell shock capturing for discontinuous

- 802 Galerkin methods. *Proc. of the 44th AIAA Aerospace Sciences Meeting and*
803 *Exhibit, AIAA-2006-112.*
- 804 Qiu, J., & Shu, C.-W. (2005). Runge–Kutta Discontinuous Galerkin Method Using
805 WENO Limiters. *SIAM Journal on Scientific Computing*, *26*, 907–929.
- 806 Rappaport, E., Franklin, J., Avila, L., Baig, S., Beven, J., Blake, E. S., ... Trib-
807 ble, A. N. (2009). Advances and challenges at the national hurricane center.
808 *Weather and Forecasting*, *24*, 395–419.
- 809 Reasor, P. D., Eastin, M. D., & Gamache, J. F. (2009). Rapidly intensifying Hurri-
810 cane Guillermo (1997). *Part I: Low-wavenumber structure and evolution. Mon.*
811 *Wea. Rev.*, *137*.
- 812 Rogers, R., Reasor, P., & Lorsolo, S. (2013). Airborne doppler observations of the
813 inner-core structural differences between intensifying and steady-state tropical
814 cyclones. *MWR*, *141*, 2970–2991.
- 815 Shapiro, L. J., & Willoughby, H. E. (1982). The response of balanced hurricanes
816 to local sources of heat and momentum. *Journal of Atmospheric Sciences*,
817 *39*(2), 378 - 394. Retrieved from [https://journals.ametsoc.org/view/](https://journals.ametsoc.org/view/journals/atsc/39/2/1520-0469_1982_039_0378_trobht_2_0_co_2.xml)
818 journals/atsc/39/2/1520-0469_1982_039_0378_trobht_2_0_co_2.xml doi:
819 10.1175/1520-0469(1982)039<0378:TROBHT>2.0.CO;2
- 820 Skamarock, W. C., & Klemp, J. B. (2008). A time-split nonhydrostatic atmo-
821 spheric model for weather research and forecasting applications. *Journal*
822 *of Computational Physics*, *227*(7), 3465 - 3485. Retrieved from [http://](http://www.sciencedirect.com/science/article/pii/S0021999107000459)
823 www.sciencedirect.com/science/article/pii/S0021999107000459 (Pre-
824 dicting weather, climate and extreme events) doi: [https://doi.org/10.1016/](https://doi.org/10.1016/j.jcp.2007.01.037)
825 [j.jcp.2007.01.037](https://doi.org/10.1016/j.jcp.2007.01.037)
- 826 Skamarock, W. C., Klemp, J. B., Dudhia, J., Gill, O., Liu, Z., Berner, J., ... yu
827 Huang, X. (2021). A description of the advanced research wrf model version 4.
828 *NCAR Technical Notes*. doi: <http://dx.doi.org/10.5065/1dfh-6p97>
- 829 Sroka, S., & Guimond, S. R. (2021). Organized kinetic energy backscatter in the
830 hurricane boundary layer from radar measurements. *Journal of Fluid Mechan-*
831 *ics*, *924*, A21. doi: 10.1017/jfm.2021.632
- 832 Takemi, T., & Rotunno, R. (2003). The effects of subgrid model mixing and numer-
833 ical filtering in simulations of mesoscale cloud systems. *Monthly Weather Re-*
834 *view*, *131*(9), 2085 - 2101. Retrieved from [https://journals.ametsoc.org/](https://journals.ametsoc.org/view/journals/mwre/131/9/1520-0493_2003_131_2085_teosmm_2_0_co_2.xml)
835 [view/journals/mwre/131/9/1520-0493_2003_131_2085_teosmm_2_0_co_2.xml](https://journals/mwre/131/9/1520-0493_2003_131_2085_teosmm_2_0_co_2.xml)
836 doi: 10.1175/1520-0493(2003)131(2085:TEOSMM)2.0.CO;2
- 837 Wang, Z. J., Fidkowski, K., Abgrall, R., Bassi, F., Caraeni, D., Cary, A., ... Visbal,
838 M. (2013). High-order cfd methods: current status and perspective. *Interna-*
839 *tional Journal for Numerical Methods in Fluids*, *72*, 811–845.
- 840 Wicker, L. J., & Skamarock, W. C. (2002). Time-Splitting Methods for Elastic
841 Models Using Forward Time Schemes. *Monthly Weather Review*, *130*(8), 2088-
842 2097. Retrieved from [https://doi.org/10.1175/1520-0493\(2002\)130<2088:](https://doi.org/10.1175/1520-0493(2002)130<2088:TSMFEM>2.0.CO;2)
843 [TSMFEM>2.0.CO;2](https://doi.org/10.1175/1520-0493(2002)130<2088:TSMFEM>2.0.CO;2) doi: 10.1175/1520-0493(2002)130(2088:TSMFEM)2.0.CO;
844 2
- 845 Yu, M. L., Giraldo, F. X., Peng, M., & Wang, Z. J. (2015). Localized Artificial
846 Viscosity Stabilization of Discontinuous Galerkin Methods for Nonhydrostatic
847 Mesoscale Atmospheric Modeling. *Monthly Weather Review*, *143*, 4823–4845.
- 848 Zhang, X., & Shu, C.-W. (2010). On positivity preserving high order discontinuous
849 galerkin schemes for compressible euler equations on rectangular meshes. *J.*
850 *Comput. Phys.*, *229*, 8918–8934.